TSINGHUA SCIENCE AND TECHNOLOGY
ISSN 1007-0214 02/10 pp9–23
DOI: 10.26599/TST.2019.9010041
Volume 26, Number 1, February 2021

Fractional-Order Proportional-Integral-Derivative Linear Active Disturbance Rejection Control Design and Parameter Optimization for Hypersonic Vehicles with Actuator Faults

Ke Gao, Jia Song*, Xu Wang, and Huifeng Li

Abstract: The hypersonic vehicle model is characterized by strong coupling, nonlinearity, and acute changes of aerodynamic parameters, which are challenging for control system design. This study investigates a novel compound control scheme that combines the advantages of the Fractional-Order Proportional-Integral-Derivative (FOPID) controller and Linear Active Disturbance Rejection Control (LADRC) for reentry flight control of hypersonic vehicles with actuator faults. First, given that the controller has adjustable parameters, the frequency-domain analysis-method-based parameter tuning strategy is utilized for the FOPID controller and LADRC method (FOLADRC). Then, the influences of the actuator model on the anti-disturbance capability and parameter tuning of the FOLADRC-based closed-loop control system are analyzed. Finally, the simulation results indicate that the proposed FOLADRC approach has satisfactory performance in terms of rapidity, accuracy, and robustness under the normal operating condition and actuator fault condition.

Key words: Active Disturbance Rejection Control (ADRC); Fractional-Order Proportional-Integral-Derivative (FOPID); Linear Extended State Observer (LESO); Near Space Hypersonic Vehicle (NSHV); actuator faults

1 Introduction

Near-Space Hypersonic Vehicles (NSHVs) have potential value in both military and civil applications and have attracted considerable attention in recent years[1]. Compared with conventional aerial vehicles, hypersonic vehicles are characterized by large envelopes, high speed, low launch cost, dynamic properties, and reusability[2]. Nonlinearity, strong coupling, and aerodynamic uncertainty may lead to large uncertain disturbances in the system. Thus, these features pose certain challenges for control system design[3].

Many control methods, such as sliding mode control, adaptive control, robust control, and other hybrid methods, have been investigated for flight control of hypersonic vehicles in the past decades. Duan and Li[4] reviewed the methodologies and summarized the challenges and limitations. The actuator plays an important role in the control system of the aircraft. Actuator faults have become an important practical problem in flight control. For attitude control, the fault-tolerant control method is a promising technique to ensure safety and reliability in the event of actuator faults[5]. A fault-tolerant control design technique against actuator stuck faults was investigated using integral-type sliding mode control with application

• Ke Gao, Jia Song, and Huifeng Li are with the School of Astronautics, Beihang University, Beijing 100191, China. E-mail: {gaoke, songjia, lihuifeng}@buaa.edu.cn.
• Xu Wang is with the School of Aerospace, Mechanical and Manufacturing Engineering, Royal Melbourne Institute of Technology University, Melbourne, Vic3083, Australia. E-mail: xu.wang@rmit.edu.au.
* To whom correspondence should be addressed.
Manuscript received: 2019-04-01; revised: 2019-08-24; accepted: 2019-08-27

to the spacecraft attitude maneuvering control system by Hu et al.[6] Lai et al.[7] proposed a new tuning-function-based control scheme for an infinite number of actuator faults. Gao and Cai[8] used the radial basis function neural network and the finite-time adaptive fault-tolerant control technique to deal with the wing flutter problem considering actuator faults. Yu et al.[9] proposed a fault-tolerant control scheme for a hypersonic gliding vehicle to counteract actuator faults and model uncertainties. A robust adaptive fault-tolerant control approach to attitude tracking of flexible spacecraft was proposed for use in situations of reaction actuator failures by Jiang et al.[10] A flexible spacecraft attitude control scheme that guarantees vibration suppression and prescribed performance on transient-state behavior was proposed considering actuator saturation faults[11]. Zhong[12] proposed a reliable active fault-tolerant tracking control system for actuator faults in a quadrotor unmanned aerial vehicle.

The Active Disturbance Rejection Control (ADRC) method was proposed by Han[13] to solve the weaknesses of traditional Proportional-Integral-Derivative (PID) control. The ADRC is a robust method and has been widely used in many applications. Gao[14] linearized the nonlinear extended state observer and proposed the Linear Extended State Observer (LESO) and Linear Active Disturbance Rejection Control (LADRC). The LADRC has a simple structure and well-developed analytical theories and has obtained satisfactory control in some fields. The Fractional-Order Proportional-Integral-Derivative (FOPID) controller, which has two additional degrees of integral order λ and proportion order μ compared with the classical PID controller, was proposed by Podlubny et al.[15] The FOPID controller and ADRC are both extensions of the classical PID controller. The FOPID can make a control system more accurate and flexible with the additional parameters, except for three essential parameters. The ADRC achieves dynamic feedback compensation for a large uncertainty covering the unknown dynamics, external disturbance, and unknown coefficients of the Extended State Observer (ESO)[16]. The Fractional-Order Active Disturbance Rejection Control (FOADRC) combines the advantages of ADRC and FOPID, which ensures that it has good control quality and high robustness and is suitable for reentry flight control of hypersonic vehicles with actuator faults. A compound control scheme that combines the advantages of the FOPID controller and nonlinear ADRC method was first applied by Qin et al.[17] to achieve hypersonic vehicle flight control. Their simulation results indicated the satisfactory performance of the controller in terms of rapidity, accuracy, and robustness. Song et al.[18,19] investigated the parameter optimization strategy of the nonlinear FOADRC method for hypersonic vehicles. To achieve efficient tracking, a comprehensive flight path regulation scheme based on ADRC was proposed for hypersonic vehicles[20]. Tian et al.[21] designed a robust output feedback autopilot for an air-breathing hypersonic vehicle based on the ADRC.

However, compared with the ADRC and FOPID methods, the FOADRC method has more tuning parameters, which increases the difficulty of parameter tuning. The parameter tuning methods for the ADRC are mainly the empirical approach and frequency-domain analysis method. Meanwhile, the parameter tuning methods for the FOPID controller are the frequency-domain analysis method, neural network algorithm, genetic algorithm, and particle swarm algorithm. In fact, some nature-inspired algorithms have already been used to solve the parameter tuning problem of the nonlinear FOADRC method. Song et al.[18] optimized the control parameters using the Nondominated Sorting Particle Swarm Optimization (NSPSO) algorithm. However, the NSPSO algorithm applied to parameter setting is only for parameters λ and μ, whereas the other parameters are still set based on experience. A compound scheme that combines the advantages of differential evolution and biogeography-based optimization was applied to optimize the control parameters, except for parameters λ and μ[19]. The frequency-domain analysis method as a classical method of control system design has been well investigated compared with the nature-inspired algorithms and is widely used for engineering applications. However, no research on the frequency-domain analysis-method-based parameter tuning strategy for the FOADRC method has been conducted until now.

In this study, a compound control scheme that combines the advantages of the FOPID controller and LADRC method (FOLADRC) is investigated for hypersonic vehicle flight control considering actuator faults. Then, the parameters of the hypersonic vehicle reentry attitude control system are optimized by the frequency-domain analysis method. Furthermore, the influences of the actuator model on the anti-disturbance capability and parameter tuning of the FOLADRC-

based closed-loop control system are analyzed. The performance of the FOLADRC, FOPID controller, and LADRC method is investigated through simulations.

The remainder of the paper is organized as follows. In Section 2, the six Degrees Of Freedom (6-DOF) model of hypersonic vehicles is presented. In Section 3, the FOLADRC method is proposed and the control parameters of the Tracking Differentiator (TD), LESO, and FOPID controller are tuned by the frequency-domain analysis method. The stability and influences of the actuator model are analyzed. In Section 4, the FOLADRC method is compared with the FOPID and ADRC methods to verify its high effectiveness and superior control performance under the normal operating condition and the actuator fault condition. Finally, Section 5 draws the conclusions.

2 Hypersonic Vehicle Model with Actuator Faults

This study on NSHV control focuses on the winged-cone model proposed by Shaughnessy et al.[22] Figure 1 shows the schematic drawing of the NSHV. Table 1 shows the parameters of the NSHV.

The notations used in the NSHV model, which were derived from the study of Song et al.[18], are shown in Fig. 2.

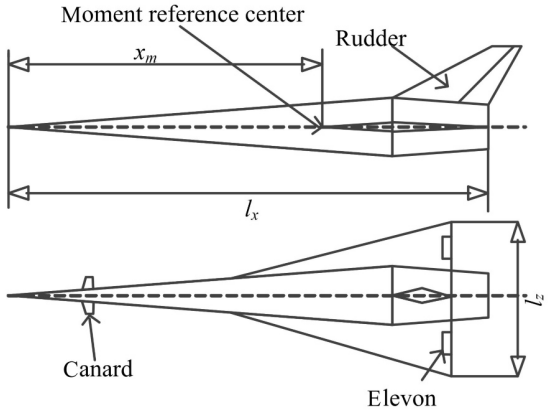

Fig. 1 Schematic drawing of the NSHV.

Table 1 Main parameters of the NSHV.

Parameter	Value
Total mass (kg)	136 820
Reference area of the wing (m)	334.730
Total length (m)	60.960
Average aerodynamic chord length (m)	24.343
Span (m)	18.288
Distance from reference torque center to leading edge (m)	37.800
Aileron reference area (m^2)	8.575
Rudder reference area (m^2)	14.990
Canard reference area (m^2)	14.335

In Fig. 2, the inertia coordinate system $ox_oy_oz_o$, speed coordinate system $ox_hy_hz_h$, and body coordinate system $ox_by_bz_b$ are depicted. F and P denote the aerodynamic force and propulsion, respectively. The angle of attack α is the angle between x_b and the plane of x_hoz_h. The sideslip angle β is the angle between x_h and the plane of x_boy_b. V represents the velocity.

Define the roll angle γ as the angle between y_b and the plane of x_oy_o. The reentry process of the NSHV can be described by the following 13 nonlinear differential equations.

$$\dot{x} = V\cos\theta\cos\psi \tag{1}$$

$$\dot{y} = V\sin\theta \tag{2}$$

$$\dot{z} = -V\cos\theta\sin\psi \tag{3}$$

$$\dot{V} = -\frac{D}{m} + \frac{g}{r}(x\cos\psi\cos\theta + (y+R)\sin\theta - z\sin\psi\cos\theta) \tag{4}$$

$$\dot{\theta} = \frac{L\cos\gamma - C\sin\gamma}{mV\cos\psi} + \frac{g}{rV\cos\psi}(-x\cos\psi\sin\theta + (y+R)\cos\theta + z\sin\psi\sin\theta) \tag{5}$$

$$\dot{\psi} = -\frac{L\sin\gamma + C\cos\gamma}{mV} - \frac{g}{rV}(x\sin\psi + z\cos\psi) \tag{6}$$

$$\dot{\omega}_x = \frac{(I_y - I_z)}{I_x}\omega_y\omega_z + \frac{1}{I_x}l \tag{7}$$

$$\dot{\omega}_y = \frac{(I_z - I_x)}{I_y}\omega_x\omega_z + \frac{1}{I_y}m \tag{8}$$

$$\dot{\omega}_z = \frac{(I_x - I_y)}{I_z}\omega_x\omega_z + \frac{1}{I_z}n \tag{9}$$

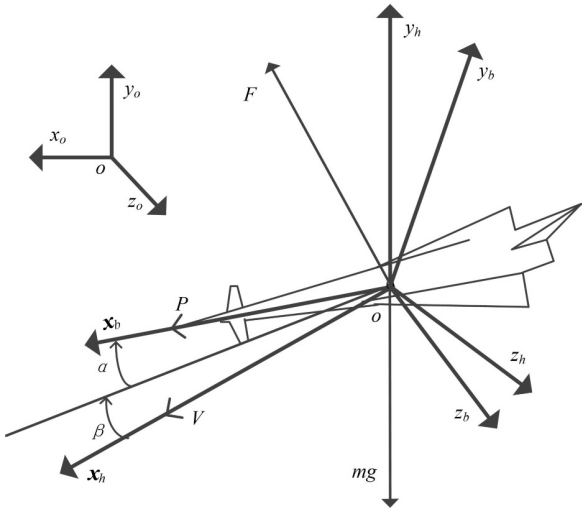

Fig. 2 Notations related to the NSHV.

$$\dot{\alpha} = \omega_z - \omega_x \cos\alpha \tan\beta + \omega_y \sin\alpha \tan\beta - \frac{1}{mV\cos\beta}(L + mg\cos\theta\cos\gamma_c) \tag{10}$$

$$\dot{\beta} = \omega_x \sin\alpha + \omega_y \cos\alpha + \frac{1}{mV}(C - mg\cos\theta\sin\gamma_c) \tag{11}$$

$$\dot{\gamma}_c = \omega_x \frac{\cos\alpha}{\cos\beta} - \omega_y \frac{\sin\alpha}{\cos\beta} + \frac{1}{mV}[L(\sin\theta\sin\gamma_c + \tan\beta) + C\sin\theta\cos\gamma_c + mg\cos\theta\cos\gamma_c\tan\beta] \tag{12}$$

$$g = g_0\left(\frac{R}{R+y}\right)^2 \tag{13}$$

where θ is the flight path angle, ψ is the flight path azimuth angle, γ_c is the velocity bank angle, g is the gravitational acceleration, g_0 is the gravity on the earth's surface, R is the earth's radius, and r is the mass center vector of the inertial coordinates. ω_x, ω_y, and ω_z represent the roll, yaw, and pitch angular rates, respectively. I_x, I_y, and I_z denote the moments of inertia for the x, y, and z coordinate axes, respectively. D, L, and C are the drag, lift, and side forces, respectively. l, m, and n represent the roll, yaw, and pitch moments, respectively.

In this study, the hypersonic vehicle is used for the reentry process without power. The main attitude control relies on the aerodynamic moments provided by the actuators, including the left aileron, the right aileron, and the rudder. The aerodynamic equations and model parameters are obtained from the study of Keshmiri et al.[23] The atmospheric model refers to the standard atmosphere in the USA in 1976. The aerodynamic model is expressed with the lift force coefficient C_L, drag force coefficient C_D, side force coefficient C_C, roll moment coefficient C_l, yaw moment coefficient C_m, and pitch moment coefficient C_n.

$$\begin{cases} L = C_L qS; \\ D = C_D qS; \\ C = C_C qS \end{cases} \tag{14}$$

$$\begin{cases} l = C_l qbS; \\ m = C_m qbS + X_{cg}C; \\ n = C_n qcS + X_{cg}(D\sin\alpha + L\cos\alpha) \end{cases} \tag{15}$$

where $q = \rho V^2/2$, ρ is the atmospheric density, S is the reference area of the wing, b is the lateral-directional reference length, X_{cg} is the longitudinal distance from momentum reference to vehicle center of gravity, and c is the average aerodynamic chord length.

The aerodynamic force and moment coefficients are calculated as follows:

$$\begin{cases} C_L = C_{L,\alpha} + C_{L,\delta_a} + C_{L,\delta_e}; \\ C_D = C_{D,\alpha} + C_{D,\delta_a} + C_{D,\delta_r} + C_{D,\delta_e}; \\ C_C = C_{C,\beta}\beta + C_{C,\delta_a} + C_{C,\delta_r} + C_{C,\delta_e} \end{cases} \tag{16}$$

$$\begin{cases} C_l = C_{l,\beta}\beta + C_{l,\delta_a} + C_{l,\delta_r} + C_{l,\delta_e} + C_{l,p}\dfrac{\omega_x b}{2V} + C_{l,r}\dfrac{\omega_y b}{2V}; \\ C_m = C_{m,\beta}\beta + C_{m,\delta_a} + C_{m,\delta_r} + C_{m,\delta_e} + C_{m,p}\dfrac{\omega_x b}{2V} + C_{m,r}\dfrac{\omega_y b}{2V}; \\ C_n = C_{n,\alpha} + C_{n,\delta_a} + C_{n,\delta_r} + C_{n,\delta_e} + C_{n,q}\dfrac{\omega_z c}{2V} \end{cases} \tag{17}$$

where $C_{L,\alpha}$, C_{L,δ_a}, and C_{L,δ_e} are lift increment coefficients for basic vehicle, right elevon, and left elevon, respectively; $C_{D,\alpha}$, C_{D,δ_a}, C_{D,δ_e}, and C_{D,δ_r} are drag increment coefficients for basic vehicle, right elevon, left elevon, and rudder, respectively; $C_{C,\beta}$ is side force with sideslip derivative for basic vehicle; C_{C,δ_a}, C_{C,δ_r}, and C_{C,δ_e} are side force increment coefficients for right elevon, left elevon, and rudder, respectively; $C_{l,\beta}$ is rolling moment with sideslip derivative for basic vehicle; C_{l,δ_a}, C_{l,δ_r}, and C_{l,δ_e} are rolling moment increments for right elevon, left elevon, and rudder, respectively; $C_{l,p}$ and $C_{l,r}$ are rolling moments with roll and yaw rate dynamic derivatives, respectively; $C_{m,\beta}$ is yawing moment with sideslip derivative for basic vehicle; C_{m,δ_a}, C_{m,δ_r}, and C_{m,δ_e} are yawing moment increment coefficients for right elevon, left elevon, and rudder, respectively; $C_{m,p}$ and $C_{m,r}$ are yawing moments with roll and yaw rate dynamic derivatives, respectively; $C_{n,\alpha}$ is pitching moment increment coefficient for basic vehicle; C_{n,δ_a}, C_{n,δ_r}, and C_{n,δ_e} are pitching moment increment coefficients for right elevon, left elevon, and rudder, respectively; $C_{n,q}$ is pitching moment pitch rate dynamic derivative.

On the basis of the data obtained from Ref. [23], the curves of the aerodynamic coefficients $C_{L,\alpha}$ and $C_{n,\alpha}$ with attack angle α and Mach (Ma) number are shown in Figs. 3 and 4, respectively.

Figure 3 shows that the aerodynamic force coefficient $C_{L,\alpha}$ increases approximately linearly with the attack angle for various Mach numbers. Figure 4 shows that the aerodynamic moment coefficient $C_{n,\alpha}$ decreases approximately linearly with the attack angle for low Mach numbers and nonlinearly with the attack angle for high Mach numbers. Obvious zero offsets exist in both $C_{L,\alpha}$ and $C_{n,\alpha}$. From Eq. (17) and Figs. 3 and

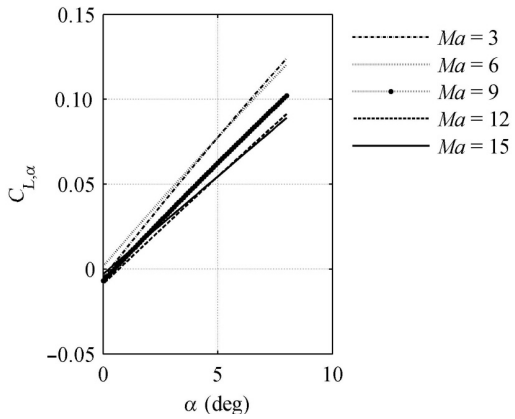

Fig. 3 Curves of the aerodynamic force coefficient $C_{L,\alpha}$.

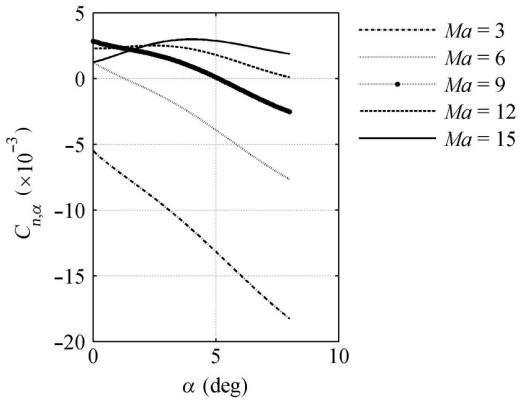

Fig. 4 Curves of the aerodynamic moment coefficient $C_{n,\alpha}$.

4, we can observe that system coupling, nonlinearity, external disturbances, and model uncertainties exist in the practical NSHV system. The uncertain features of hypersonic vehicles may lead to reentry flight control difficulty.

Before control schemes are planned and designed, the hypersonic vehicle model must be linearized. Moreover, the variables $\dot{\alpha} = F_a$, $\dot{\beta} = F_\beta$, and $\dot{\gamma}_c = F_{\gamma_c}$ must be defined. By linearizing the hypersonic vehicle model, the second derivative of the attack, sideslip, and bank angles can be written as follows:

$$\ddot{\alpha} = \frac{\partial F_\alpha}{\partial \alpha}\alpha + \frac{\partial F_\alpha}{\partial \dot{\alpha}}\dot{\alpha} + \left.\frac{\partial F_\alpha}{\partial \delta_a}\right|_{\delta_a=0}\delta_\alpha + f_\alpha \tag{18}$$

$$\ddot{\beta} = \frac{\partial F_\beta}{\partial \beta}\beta + \frac{\partial F_\beta}{\partial \dot{\beta}}\dot{\beta} + \left.\frac{\partial F_\beta}{\partial \delta_r}\right|_{\delta_r=0}\delta_\beta + f_\beta \tag{19}$$

$$\ddot{\gamma}_c = \frac{\partial F_{\gamma_c}}{\partial \gamma_c}\gamma_c + \frac{\partial F_{\gamma_c}}{\partial \dot{\gamma}_c}\dot{\gamma}_c + \left.\frac{\partial F_{\gamma_c}}{\partial \delta_a}\right|_{\delta_a=0}\delta_{\gamma_c} + f_{\gamma_c} \tag{20}$$

where

$$\begin{pmatrix}\delta_\alpha\\ \delta_\beta\\ \delta_{\gamma_c}\end{pmatrix} = \begin{pmatrix}1 & 0 & 1\\ 0 & 1 & 0\\ 1 & 0 & -1\end{pmatrix}\begin{pmatrix}\delta_a\\ \delta_r\\ \delta_e\end{pmatrix},$$

$$f_\alpha = \frac{qcS}{I_z}C_{n,\delta_r} + \Delta_\alpha,$$

$$f_\beta = \frac{qS}{I_y}\left(b\left(C_{m,\delta_a} + C_{m,\delta_e} + C_{m,p}\frac{\omega_x b}{2V}\right) + X_{cg}(C_{C,\delta_a} + C_{C,\delta_e})\right) + \Delta_\beta,$$

$$f_{\gamma_c} = \frac{qbS}{I_x}\left(C_{l,\beta}\beta + C_{l,\delta_r} + C_{l,r}\frac{\omega_y b}{2V}\right) + \Delta_{\gamma_c},$$

where Δ_α, Δ_β, and Δ_{γ_c} represent the model errors and unknown disturbances.

The actuator fault model can be expressed as $\delta_f = \delta - E\delta + \bar{\delta}$. $\delta_f = [\,\delta_{af}\ \delta_{rf}\ \delta_{ef}\,]^{\mathrm{T}}$ represents the fault outputs; $\delta = [\,\delta_a\ \delta_r\ \delta_e\,]^{\mathrm{T}}$; $E = \mathrm{diag}\{E_a, E_r, E_e\} \in \mathbf{R}^{3\times 3}$ denotes the failure indicator for the actuators; and $\bar{\delta} \in \mathbf{R}^3$ represents the actuator bias faults.

Furthermore, to depict the hypersonic vehicle dynamic more clearly, the inputs and states are defined as follows:

$$\boldsymbol{x} = \begin{pmatrix}\alpha\\ \beta\\ \gamma\\ \dot{\alpha}\\ \dot{\beta}\\ \dot{\gamma}\end{pmatrix}, \boldsymbol{u} = \begin{pmatrix}\delta_\alpha\\ \delta_\beta\\ \delta_{\gamma_c}\end{pmatrix}, \boldsymbol{y} = \begin{pmatrix}\alpha\\ \beta\\ \gamma\end{pmatrix} \tag{21}$$

Then, the attitude motion equation of hypersonic vehicle can be rewritten in the following state-space form:

$$\dot{\boldsymbol{x}} = \boldsymbol{A}\boldsymbol{x} + \boldsymbol{B}\boldsymbol{u} + \boldsymbol{f} \tag{22}$$

where

$$\boldsymbol{A} = \begin{pmatrix}0 & \cdots & 0 & 1 & 0 & 0\\ \vdots & & & \ddots & 1 & 0\\ 0 & \cdots & \cdots & \cdots & 0 & 1\\ -a_{1,\alpha} & 0 & 0 & -a_{0,\alpha} & 0 & 0\\ 0 & -a_{1,\beta} & 0 & 0 & -a_{0,\beta} & 0\\ 0 & 0 & -a_{1,\gamma_c} & 0 & 0 & -a_{0,\gamma_c}\end{pmatrix},$$

$$\boldsymbol{B} = \begin{pmatrix}0 & \cdots & 0\\ \vdots & & \vdots\\ 0 & & \vdots\\ b_{0,\alpha} & \ddots & \vdots\\ 0 & b_{0,\beta} & 0\\ 0 & 0 & b_{0,\gamma_c}\end{pmatrix}, \boldsymbol{f} = \begin{pmatrix}0\\ 0\\ 0\\ f_\alpha\\ f_\beta\\ f_{\gamma_c}\end{pmatrix},$$

$$a_{0,\alpha} = \frac{\partial F_\alpha}{\partial \dot{\alpha}}, a_{1,\alpha} = \frac{\partial F_\alpha}{\partial \alpha}, a_{0,\beta} = \frac{\partial F_\beta}{\partial \dot{\beta}}, a_{1,\beta} = \frac{\partial F_\beta}{\partial \beta},$$

$$a_{0,\gamma_c} = \frac{\partial F_{\gamma_c}}{\partial \dot{\gamma}_c}, a_{1,\gamma_c} = \frac{\partial F_{\gamma_c}}{\partial \gamma_c}, b_{0,\alpha} = 2\left.\frac{\partial F_\alpha}{\partial \delta_a}\right|_{\delta_a=0},$$

$$b_{0,\beta}=\left.\frac{\partial F_\beta}{\partial \delta_r}\right|_{\delta_r=0}, b_{0,\gamma_c}=2\left.\frac{\partial F_{\gamma_c}}{\partial \delta_a}\right|_{\delta_a=0}.$$

Notably, each dimensional hypersonic vehicle model can be considered a second-order system, which is the basis of LADRC controller design.

3 FOLADRC Method for Hypersonic Vehicles with the Actuator Model

In this section, the FOLADRC method is designed for reentry flight altitude control and the control parameters of the FOADRC method are tuned by the frequency domain analysis method. The influences of the actuator model on the anti-disturbance capability and parameter tuning of the FOLADRC-based closed-loop control system are analyzed.

3.1 FOLADRC design

The conventional ADRC is composed of a TD, a PID controller, and an ESO. The TD can coordinate the contradiction between rapidity and overshoot. The ESO regards all of the disturbances as "unknown disturbances" and estimates them. The ADRC structural diagram of the hypersonic vehicle for three-axis attitude control is shown in Fig. 5.

In Fig. 5, the desired angle r^* is the input signal and y is the output signal. The structure inside the dashed frame is the controller. The controlled plant GHV is the model of a General Hypersonic Vehicle (GHV). b is the estimated control gain of GHV. z_1, z_2, and z_3 are the estimated angle, estimated derivative signal of the angle, and estimated "unknown disturbances" of the GHV obtained from the ESO, respectively. u_0 is the ideal control variable and u is the actual control variable. Then, the TD and ESO are introduced.

The TD discrete form can be described by the following equations:

$$\begin{aligned}&\alpha_1(k+1)=\alpha_1(k)+h\alpha_2(k),\\&\alpha_2(k+1)=\alpha_2(k)+h((-r^2\alpha_1(k)-\alpha^*(k))-\\&\qquad 2r\alpha_2(k))\end{aligned}\tag{23}$$

where $\alpha_1(k)$ and $\alpha_1(k+1)$ denote the estimated angle values of the current time and next time, respectively.

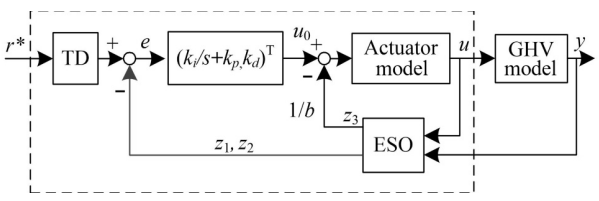

Fig. 5 ADRC structural diagram of the hypersonic vehicle.

$\alpha_2(k)$ and $\alpha_2(k+1)$ are the derivatives of $\alpha_1(k)$ and $\alpha_1(k+1)$, respectively. r and h represent the speed factor and filtering factor, respectively. The larger the value of r, the shorter the transition processes and the faster the response. The larger the value of h, the better the noise filtering. The ESO for each dimensional hypersonic vehicle model can be formulated as the following third-order system:

$$\begin{cases}e_1=z_1-y;\\ \dot{z}_1=z_2-\beta_1\mathrm{fal}(e_1,\chi_1,\delta);\\ \dot{z}_2=z_3-a_1z_1-a_0z_2+b_0u-\beta_2\mathrm{fal}(e_1,\chi_2,\delta);\\ \dot{z}_3=-\beta_3\mathrm{fal}(e_1,\chi_3,\delta)\end{cases}\tag{24}$$

where β_1, β_2, and β_3 are adjustable parameters with different values.

$$\mathrm{fal}(e,\chi,\delta)=\begin{cases}|e|^\chi\mathrm{sign}(e), & |e|>\delta;\\ \delta^{\chi-1}e, & \text{otherwise},\end{cases}$$
$$0\leqslant\chi\leqslant 1,\delta>0\tag{25}$$

The FOLADRC is adopted to solve the hypersonic vehicle control problem in this study. Compared with the conventional ADRC, the FOLADRC replaces the PID controller with the FOPID controller and the ESO with the LESO. The FOLADRC structural diagram of the hypersonic vehicle for three-axis attitude control is shown in Fig. 6.

In Fig. 6, the TD, FOPID, and LESO inside the dashed frame form the controller. Then, the TD, FOPID controller, and LESO are designed.

The design of the TD is almost the same as that of the ADRC. The only difference is that only $\alpha_1(k)$ is used in the FOLADRC.

The FOPID can make a control system more accurate and flexible with the additional parameters λ and μ. Then, we simulated how the parameters λ and μ affect the FOPID controller. We set $k_p=10$, $k_i=1$, and $k_d=1$. Figures 7 and 8 give the Bode diagrams of the Fractional-Order Proportional-Integral (FOPI) and Fractional-Order Proportional-Derivative (FOPD) controllers with different values of λ and μ, respectively.

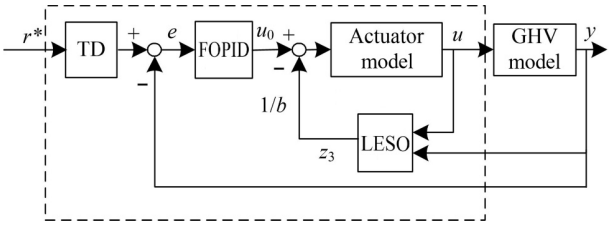

Fig. 6 FOLADRC structural diagram of the hypersonic vehicle.

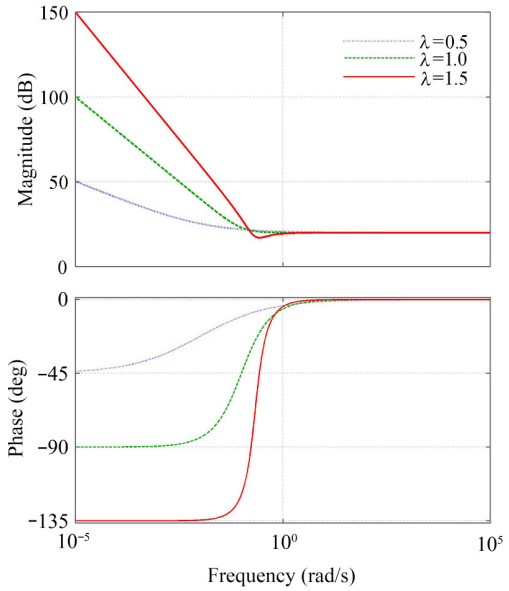

Fig. 7 Bode diagram of the FOPI controller with different values of λ.

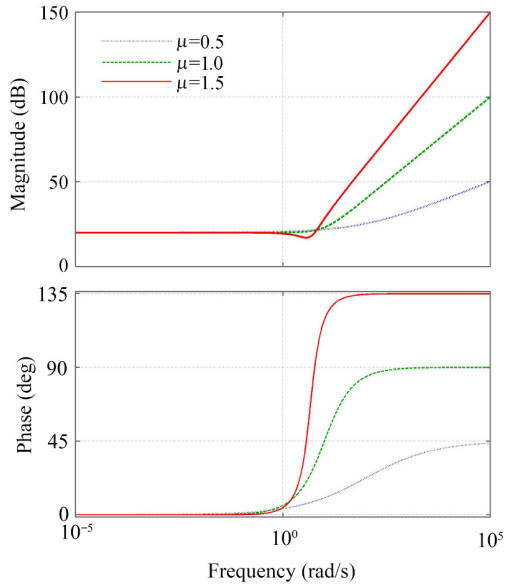

Fig. 8 Bode diagram of the FOPD controller with different values of μ.

In Fig. 7, when $\lambda = 1$, the FOPI controller is equivalent to a PI controller. In Fig. 8, when $\mu = 1$, the FOPD controller is equivalent to a PD controller. Figures 7 and 8 show that the FOPID increases the ranges of the phase frequency characteristic curves and the octave slopes of the amplitude frequency characteristic curves.

To improve the dynamic properties of middle frequency bands and obtain a simple derivation for parameter tuning, the FOPID is calculated as follows:

$$G_c(s) = K_p\left(1 + \frac{K_i}{K_p}s^{-\lambda}\right)\left(1 + \frac{K_d}{K_p}s^{\mu}\right) \tag{26}$$

where λ and μ are restricted to $0 < \lambda < 2$ and $0 < \mu < 2$, respectively. The FOPID controller increases the variables λ and μ by 2-DOF, thus enabling more precise and stable control. The structural diagram of the FOPID controller is shown in Fig. 9.

The ESO used in this study is the LESO. For Eq. (25), if we take $\chi_i = 1, i = 1, 2$, and 3, then Eq. (24) becomes an LESO and it is rewritten as follows:

$$\begin{cases} e_1 = z_1 - \alpha; \\ \dot{z}_1 = z_2 - \beta_1 e_1; \\ \dot{z}_2 = z_3 - a_1 z_1 - a_0 z_2 + b_0 u - \beta_2 e_1; \\ \dot{z}_3 = -\beta_3 e_1 \end{cases} \tag{27}$$

Only the estimated "unknown disturbances" of the GHV z_3 is used in the designed FOLADRC. The estimated angle z_1 and the estimated derivative signal of the angle z_2 are not used.

The design of the TD, FOPID controller, and LESO is completed.

3.2 FOLADRC stability analysis

From Eq. (27), the LESO can be described by the state-space form,

$$\dot{z} = (\boldsymbol{A}_e - \boldsymbol{L}_0\boldsymbol{C}_e)z(t) + \boldsymbol{B}_e u(t) + \boldsymbol{L}_0 y(t) \tag{28}$$

where

$$\boldsymbol{A}_e = \begin{bmatrix} 0 & 1 & 0 \\ -\bar{a}_1 & -\bar{a}_0 & 1 \\ 0 & 0 & 0 \end{bmatrix}, \boldsymbol{B}_e = [\,0 \quad \bar{b}_0 \quad 0\,]^{\mathrm{T}}, \boldsymbol{C}_e = [\,1 \quad 0 \quad 0\,], \boldsymbol{L}_0 = [\,\beta_1 \quad \beta_2 \quad \beta_3\,]^{\mathrm{T}}.$$

By taking the Laplace transform of Eq. (28), we can derive the following expression:

$$Z_3(s) = G_{ZU}(s)U(s) + G_{ZY}(s)Y(s) \tag{29}$$

where

$$G_{ZU}(s) = -\frac{\bar{b}_0\omega_c^3}{(s+\omega_c)^3},$$

$$G_{ZY}(s) = \frac{\omega_c^3(s^2 + \bar{a}_0 s + \bar{a}_1)}{(s+\omega_c)^3}.$$

The FOLADRC structural diagram of a second-order system with the actuator model is shown in Fig. 10.

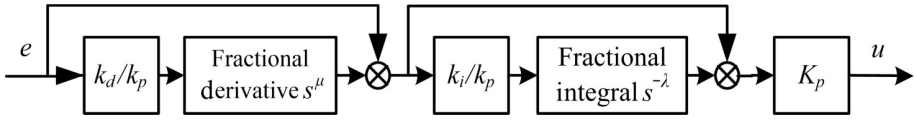

Fig. 9 Structural diagram of the FOPID controller.

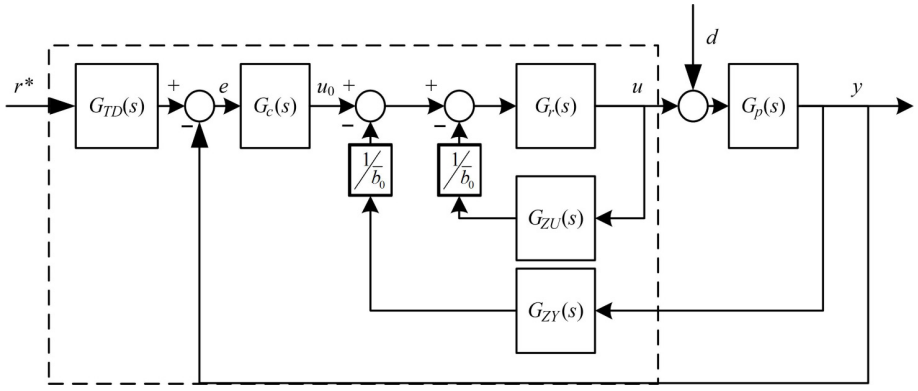

Fig. 10 Transferred FOLADRC structural diagram of a second-order system.

From Fig. 10, we can derive the transfer functions from $R(s)$ to $Y(s)$ and from $D(s)$ to $Y(s)$, respectively, as shown in Eqs. (30) and (31),

$$\frac{Y(s)}{R(s)}=\frac{G_c(s)G_r(s)G_p(s)G_{TD}(s)}{1+G_c(s)G_r(s)G_p(s)+\frac{1}{\bar{b}_0}G_r(s)(G_{ZU}(s)+G_{ZY}(s)G_p(s))} \tag{30}$$

$$\frac{Y(s)}{D(s)}=\frac{G_p(s)G_{lc}(s)}{1+G_c(s)G_r(s)G_p(s)+\frac{1}{\bar{b}_0}G_r(s)(G_{ZU}(s)+G_{ZY}(s)G_p(s))} \tag{31}$$

where

$$G_p(s)=\frac{b_0}{s^2+a_0s+a_1},\ G_r(s)=\frac{\omega_n^2}{s^2+2\xi\omega_n s+\omega_n^2},$$
$$G_{TD}(s)=\frac{r^2}{(s+r)^2},\ G_{lc}(s)=1+\frac{1}{\bar{b}_0}G_{ZU}(s)G_r(s).$$

In this study, we take $\xi = 0.9$ and $\omega_n = 98$ rad for the actuator model.

Notably, the closed-loop control system is stable if and only if all poles of the closed system transfer functions Eqs. (30) and (31) are on the left side of the complex plane. $-G_{ZU}(s)/\bar{b}_0$ and $G_r(s)$ are both low-pass filters. $G_{lc}(s)$ is a low-cut filter, thus ensuring that the LADRC achieves a strong anti-disturbance capability and high robustness. We can observe that the larger the values of the bandwidths of the LESO and actuator are, the stronger the anti-disturbance capability of the LADRC is. Furthermore, as the bandwidth of the actuator is fixed, when the value of the bandwidth of the LESO is larger than that of the actuator, the anti-disturbance capability increases only slightly. The value of the bandwidth of the LESO is limited by the actuator.

3.3 FOLADRC parameter tuning

In this section, the parameter tuning of the FOPID, ESO, and TD are investigated.

First, we discuss the parameter tuning of the FOPID controller. The FOPID control closed-loop system structure diagram is shown in Fig. 11.

In Fig. 11, G_c represents the FOPID controller, G_r represents the actuator model, and G_p represents the controlled object model. The five control parameters of the FOPID controller are k_p, k_i, k_d, λ, and μ. Five constraints are required to complete parameter tuning. In this study, the constraints to the FOPID open-loop transfer function, including the amplitude, phase angle, derivative of the phase angle at the cutoff frequency, and the amplitude and phase angle at the phase crossover frequency, are considered. The amplitude and phase angle constraints at the cutoff frequency represent the phase margin. The amplitude and phase angle constraints at the phase crossover frequency represent the amplitude margin. The derivative of the phase angle at the cutoff frequency represents the robustness of the FOPID closed-loop control system.

The amplitude and phase angle constraint equations at the cutoff frequency are expressed as follows:

$$\begin{cases} \left|G_c(\mathrm{j}\omega_c)G_r(\mathrm{j}\omega_c)G_p(\mathrm{j}\omega_c)\right| = 0\,\mathrm{dB}; \\ \arg(G_c(\mathrm{j}\omega_c)G_r(\mathrm{j}\omega_c)G_p(\mathrm{j}\omega_c)) = \pi+\varphi_m, \end{cases}$$

where ω_c is the expected cutoff frequency and φ_m is the expected phase margin.

The derivative constraint equation of the phase angle

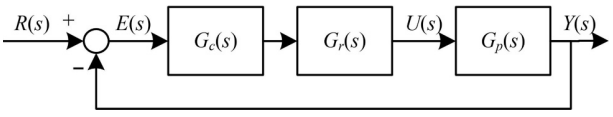

Fig. 11 FOPID closed-loop control system structure diagram.

at the cutoff frequency is expressed as follows:

$$\frac{\mathrm{d}(\arg(G_c(\mathrm{j}\omega_c)G_r(\mathrm{j}\omega_c)G_p(\mathrm{j}\omega_c)))}{\mathrm{d}w} = 0.$$

The amplitude and phase angle constraint equations at the phase crossover frequency are expressed as follows:

$$\begin{cases} \left|G_c(\mathrm{j}\omega_p)G_r(\mathrm{j}\omega_p)G_p(\mathrm{j}\omega_p)\right| = A_m \text{ dB}; \\ \arg(G_c(\mathrm{j}\omega_p)G_r(\mathrm{j}\omega_p)G_p(\mathrm{j}\omega_p)) = -\pi, \end{cases}$$

where ω_p is the expected phase crossover frequency and A_m is the expected amplitude margin.

Substituting $s = \mathrm{j}\omega$ into Eq. (26), we can derive the following expression:

$$G_c(\mathrm{j}\omega) = K_p\left(1+\frac{K_i}{K_p}(\mathrm{j}\omega)^{-\lambda}\right)\left(1+\frac{K_d}{K_p}(\mathrm{j}\omega)^{\mu}\right) \quad (32)$$

Using Euler's Formula, we can derive the following expression:

$$\mathrm{j}^a = [\mathrm{j}^2]^{\frac{\alpha}{2}} = [\left|\mathrm{j}^2\right| \mathrm{e}^{\mathrm{j}\pi}]^{\frac{\alpha}{2}} = \mathrm{e}^{\mathrm{j}\frac{\alpha\pi}{2}} = \cos\frac{\alpha\pi}{2} + \mathrm{j}\sin\frac{\alpha\pi}{2} \quad (33)$$

Substituting Eq. (33) into Eq. (32), we can derive the following expression:

$$G_c(\mathrm{j}\omega) = K_p\left(1+\frac{K_i}{K_p}\omega^{-\lambda}\cos\frac{\lambda\pi}{2} - \frac{K_i}{K_p}\omega^{-\lambda}\sin\frac{\lambda\pi}{2}\right)\cdot \left(1+\frac{K_d}{K_p}\omega^{\mu}\cos\frac{\mu\pi}{2} + \frac{K_d}{K_p}\omega^{\mu}\sin\frac{\mu\pi}{2}\right).$$

Then, we can obtain the amplitude and phase angle functions of the FOPID controller as follows:

$$|G_c(\mathrm{j}\omega)| = K_p\left|1+\frac{K_i}{K_p}s^{-\lambda}\right|\left|1+\frac{K_d}{K_p}s^{\mu}\right|,$$

$$\arg[G_c(\mathrm{j}\omega)] = \arctan\left(\frac{-K_i\omega^{-\lambda}\sin\frac{\lambda\pi}{2}}{K_p + K_i\omega^{-\lambda}\cos\frac{\lambda\pi}{2}}\right) + \arctan\left(\frac{K_d\omega^{\mu}\sin\frac{\mu\pi}{2}}{K_p + K_d\omega^{\mu}\cos\frac{\mu\pi}{2}}\right),$$

where

$$\left|1+\frac{K_d}{K_p}s^{\mu}\right| = \frac{1}{K_p}\sqrt{\left(K_p + K_d\omega^{\mu}\cos\frac{\mu\pi}{2}\right)^2 + \left(K_d\omega^{\mu}\sin\frac{\mu\pi}{2}\right)^2},$$

$$\left|1+\frac{K_i}{K_p}s^{-\lambda}\right| = \frac{1}{K_p}\sqrt{\left(K_p + K_i\omega^{-\lambda}\cos\frac{\lambda\pi}{2}\right)^2 + \left(K_i\omega^{-\lambda}\sin\frac{\lambda\pi}{2}\right)^2}.$$

The derivative of the FOPID controller phase angle function can be calculated as follows:

$$\frac{\mathrm{d}}{\mathrm{d}\omega}(\arg[G_c(\mathrm{j}\omega)]) = \frac{\mathrm{d}}{\mathrm{d}\omega}\left(\arg\left(1+\frac{K_i}{K_p}s^{-\lambda}\right)\right) + \frac{\mathrm{d}}{\mathrm{d}\omega}\left(\arg\left(1+\frac{K_d}{K_p}s^{\mu}\right)\right),$$

$$\frac{\mathrm{d}}{\mathrm{d}\omega}(\arg[G_c(\mathrm{j}\omega)]) = \frac{1}{\left|\left(1+\frac{K_i}{K_p}s^{-\lambda}\right)\right|^2}\times \left(\frac{K_i}{K_p}\lambda\omega^{-\lambda-1}\sin\frac{\lambda\pi}{2}\right) + \frac{1}{\left|\left(1+\frac{K_d}{K_p}s^{\mu}\right)\right|^2}\left(\frac{K_d}{K_p}\mu\omega^{\mu-1}\sin\frac{\mu\pi}{2}\right).$$

The controlled object model transfer function $G_p(s)$ is expressed as follows:

$$G_p(s) = \frac{\bar{b}_0}{s^2 + \bar{a}_0 s + \bar{a}_1},$$

where $\bar{a}_0$, $\bar{a}_1$, and $\bar{b}_0$ are the parameters of the nominal model of Eq. (22).

The amplitude and phase angle functions of $G_p(s)$ are derived as follows:

$$\left|G_p(\mathrm{j}\omega)\right| = \frac{\left|\bar{b}_0\right|}{\sqrt{(\omega^2 - \bar{a}_1)^2 + (\bar{a}_0\omega)^2}},$$

$$\arg(G_p(\mathrm{j}\omega)) = \arctan\left(\frac{-\bar{a}_0\omega}{-\omega^2 + \bar{a}_1}\right).$$

The derivative of the controlled object model phase angle function is calculated as follows:

$$\frac{\mathrm{d}}{\mathrm{d}\omega}(\arg[G_p(\mathrm{j}\omega)]) = \frac{-a_0a_1 - a_0\omega^2}{(-\omega^2 + a_1)^2 + (a_0\omega)^2}.$$

The actuator model transfer function $G_r(s)$ is expressed as follows:

$$G_r(s) = \frac{\omega_n^2}{s^2 + 2\xi\omega_n s + \omega_n^2}.$$

The amplitude and phase angle functions of $G_r(s)$ are derived as follows:

$$|G_r(\mathrm{j}\omega)| = \frac{\left|\omega_n^2\right|}{\sqrt{(\omega^2 - \omega_n^2)^2 + (2\xi\omega_n\omega)^2}},$$

$$\arg(G_r(\mathrm{j}\omega)) = \arctan\left(\frac{-2\xi\omega_n\omega}{-\omega^2 + \omega_n^2}\right).$$

The derivative of the actuator model phase angle function is calculated as follows:

$$\frac{\mathrm{d}}{\mathrm{d}\omega}(\arg[G_r(\mathrm{j}\omega)]) = \frac{-2\xi\omega_n^3 - 2\xi\omega_n\omega^2}{(-\omega^2 + \omega_n^2)^2 + (2\xi\omega_n\omega)^2}.$$

Eventually, the five constraint equations are expressed in Eq. (34).

$$\begin{cases} |G_c(\mathrm{j}\omega_c)||G_r(\mathrm{j}\omega_c)||G_p(\mathrm{j}\omega_c)| = 1; \\ \arg(G_c(\mathrm{j}\omega_c))+\arg(G_r(\mathrm{j}\omega_c))+\arg(G_p(\mathrm{j}\omega_c))= \\ \quad \pi+\varphi_m; \\ |G_c(\mathrm{j}\omega_p)||G_r(\mathrm{j}\omega_p)||G_p(\mathrm{j}\omega_p)| = A_m; \\ \arg(G_c(\mathrm{j}\omega_p))+\arg(G_r(\mathrm{j}\omega_p))+\arg(G_p(\mathrm{j}\omega_p))= -\pi; \\ \dfrac{\mathrm{d}}{\mathrm{d}\omega}(\arg[G_c(\mathrm{j}\omega)])+\dfrac{\mathrm{d}}{\mathrm{d}\omega}(\arg[G_r(\mathrm{j}\omega)])+ \\ \quad \dfrac{\mathrm{d}}{\mathrm{d}\omega}(\arg[G_p(\mathrm{j}\omega)]) = 0 \end{cases} \tag{34}$$

As it is difficult to solve nonlinear equations, such as Eq.(34), the nonlinear optimization function fmincon of the MATLAB optimization toolbox is used to obtain the control parameters k_p, k_i, k_d, λ, and μ. We take the derivative of the phase angle at the cutoff frequency as the objective function, the cutoff frequency and phase margin as the nonlinear equality constraints, and the phase crossover frequency and amplitude margin as the nonlinear inequality constraints. The objective function is expressed as follows:

$$J = \left(\frac{\mathrm{d}}{\mathrm{d}\omega}(\arg(G_c(\mathrm{j}\omega))) + \frac{\mathrm{d}}{\mathrm{d}\omega}(\arg(G_r(\mathrm{j}\omega)))+ \frac{\mathrm{d}}{\mathrm{d}\omega}(\arg(G_p(\mathrm{j}\omega)))\right)^2.$$

The nonlinear equality constraints are expressed as follows:

$$\begin{cases} |G_c(\mathrm{j}\omega_c)|\,|G_r(\mathrm{j}\omega_c)|\,\left|G_p(\mathrm{j}\omega_c)\right| = 1; \\ \arg(G_c(\mathrm{j}\omega_c)) + \arg(G_r(\mathrm{j}\omega_c)) + \arg(G_p(\mathrm{j}\omega_c)) = \\ \quad \pi + \varphi_m; \\ \arg(G_c(\mathrm{j}\omega_p)) + \arg(G_r(\mathrm{j}\omega_p)) + \arg(G_p(\mathrm{j}\omega_p)) = \\ \quad -\pi. \end{cases}$$

The nonlinear inequality constraints are expressed as follows:

$$\begin{cases} \omega_p < \omega_{pr}; \\ \left|G_c(\mathrm{j}\omega_p)\right|\left|G_r(\mathrm{j}\omega_p)\right|\left|G_p(\mathrm{j}\omega_p)\right| - A_m > 0, \end{cases}$$

where ω_p is the actual phase crossover frequency and ω_{pr} is the maximum value set for the phase crossover frequency.

The value of k_p is mainly determined by the cutoff frequency ω_c. The values of k_d and μ are mainly determined by the phase margin and derivative of the phase angle at the cutoff frequency. The values of k_i and λ are mainly determined by the phase crossover frequency and amplitude margin. Particularly for the yaw channel, the parameters k_i and λ are set to zero. The nonlinear equality constraints are the phase margin and cutoff frequency equations. Then, the values of the parameters $[k_p, k_i, k_d, \lambda, \mu]$ for the pitch, yaw, and roll channels are [36.16, 8.31, 1.38, 1.07, 1.25], [−27.82, 0, −2.79, 0, 1.11], and [2.91, 0.17, 0.32, 1.2, 1.1], respectively. The bode diagrams of the FOPID controllers for the pitch, yaw, and roll channels are shown in Figs. 12 – 14, respectively.

In Figs. 12 – 14, we can observe that the derivative values of the phase angle at the cutoff frequency are

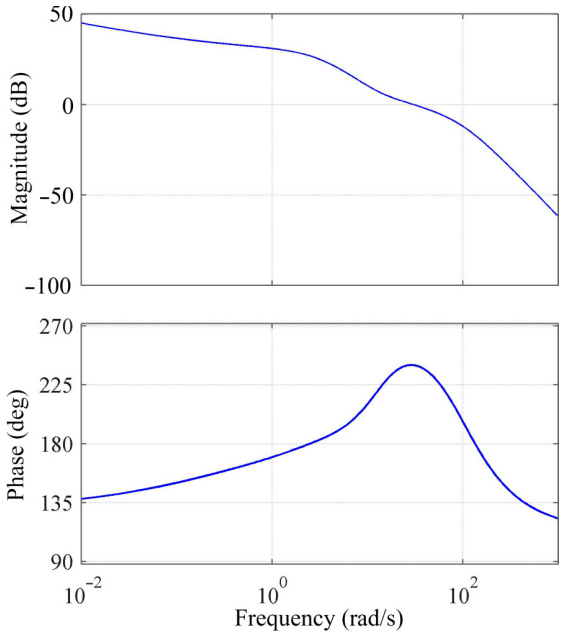

Fig. 12 Bode diagram of the FOPID controller for the pitch channel.

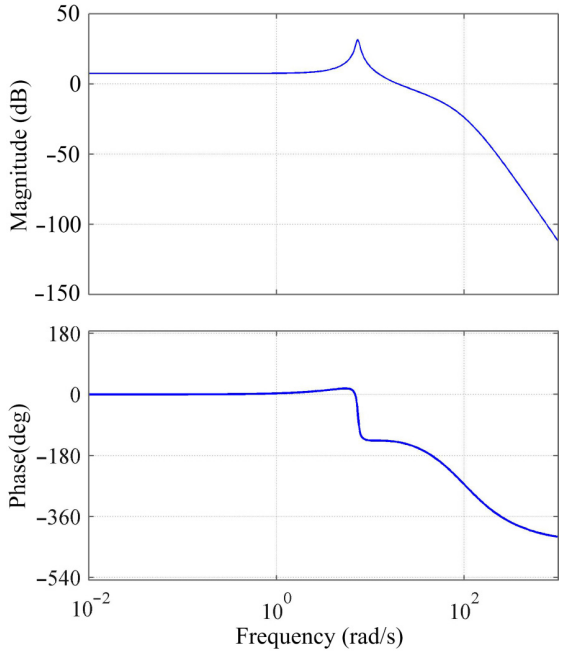

Fig. 13 Bode diagram of the FOPID controller for the yaw channel.

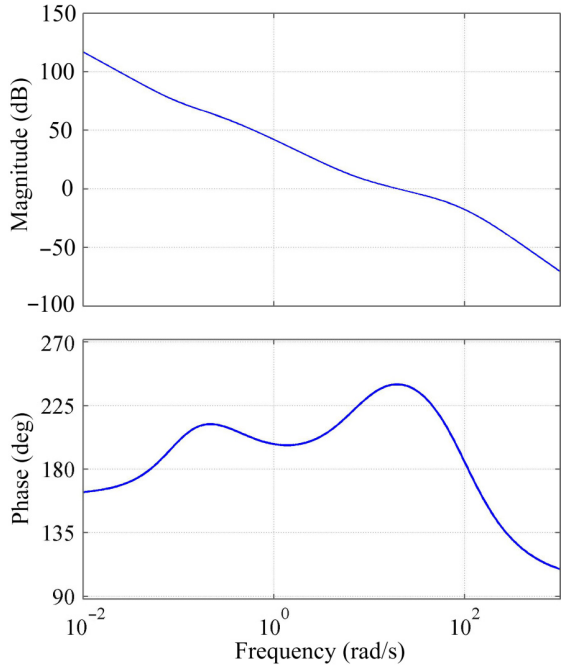

Fig. 14 Bode diagram of the FOPID controller for the roll channel.

nearly zero. The cutoff frequencies and phase margins satisfy the nonlinear equality constraints. The phase crossover frequencies and amplitude margins satisfy the nonlinear inequality constraints.

Second, we introduce the parameter tuning method for the TD. The TD continuous form can be described by the following equation:

$$\begin{cases} \dot{\alpha}_1 = \alpha_2; \\ \dot{\alpha}_2 = -r^2\alpha_1 - 2r\alpha_2 + r^2\alpha^*. \end{cases}$$

Then, we can derive the following expression:

$$\alpha_1 = \frac{r^2}{(s+r)^2}\alpha^*.$$

The r value can be obtained on the basis of the cutoff frequency of the FOPID open-loop or closed-loop transfer function. Particularly, when the amplitude margin of the FOPID open-loop transfer function φ_m is 60°, the cutoff frequency of the FOPID open-loop transfer function is equal to that of the FOPID closed-loop transfer function. In this study, we take 60° as the value of φ_m, the sampling period of the control system as the value of h, and the cutoff frequency of the FOPID open-loop transfer function as the value of r.

Finally, we consider the parameter tuning of the LESO. The LESO parameters can be tuned on the basis of the cutoff frequency of the FOPID closed-loop control system. The LESO parameters can be derived as follows:

$$\begin{aligned} \beta_1 &= 3(m_\beta\omega_c) - \bar{a}_0, \\ \beta_2 &= 3(m_\beta\omega_c)^2 - \bar{a}_1 - \bar{a}_0\beta_1, \\ \beta_3 &= (m_\beta\omega_c)^3, \end{aligned}$$

where m_β is a constant value.

Thus, parameter tuning of the TD, FOPID controller, and LESO is completed.

4 Simulation

4.1 Simulation of the FOLADRC under the normal operating condition

The initial output parameters are $[V, \theta, \psi_c, \omega_x, \omega_y, \omega_z, \alpha, \beta, \gamma_c, x, y, z] = [15\ Ma, 0, 0, 0, 0, 0, 0, 0, 0, 0, 33\,500\ \text{m}, 0]$. The initial actuator parameters are $[\delta_e, \delta_a, \delta_r] = [0, 0, 0]$. The desired attack and bank angles for the control system are continuous square wave signals with amplitudes of 1° and 10°, respectively. The desired sideslip angle for the control system is zero. The LADRC and FOPID methods are designed and compared. The parameters of the FOPID controller are the same for the FOPID and FOLADRC methods. The parameters of the LESO are the same for the LADRC and FOLADRC methods. The simulation results of the LADRC, FOPID, and FOLADRC methods are shown in Figs. 15 – 19. The performance parameters (for the first step input signal) of the three controllers are shown in Table 2.

In Figs. 15 and 16, we can observe that the FOLADRC controller has the smallest steady-state error, settling time, and overshoot compared with the FOPID and LADRC controllers. In Fig. 17, we can easily observe that the LADRC and FOLADRC

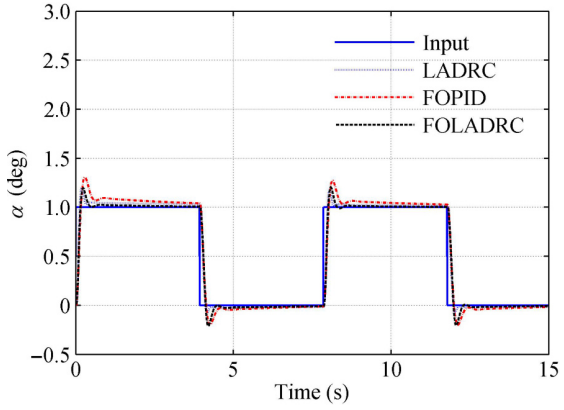

Fig. 15 Output responses of tracking the desired attack angle.

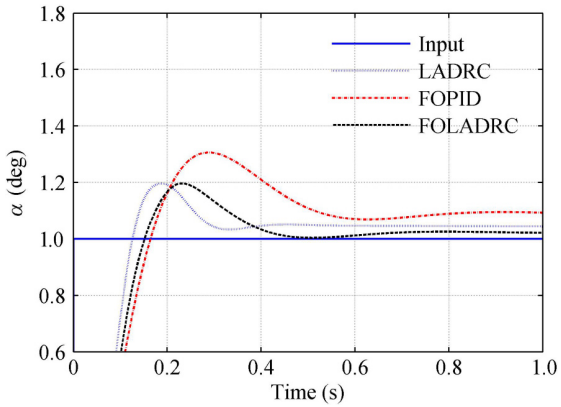

Fig. 16 Output responses of tracking the desired attack angle (partial enlargement).

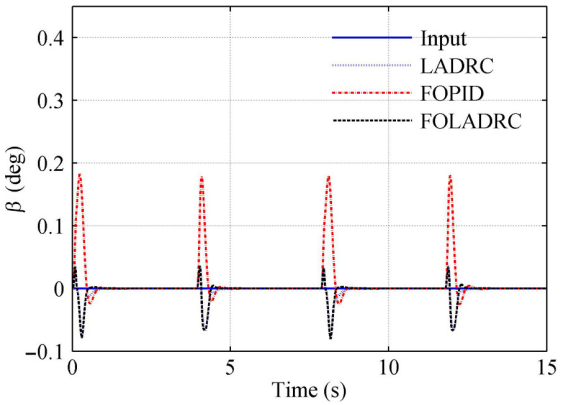

Fig. 17 Output responses of tracking the desired sliding angle.

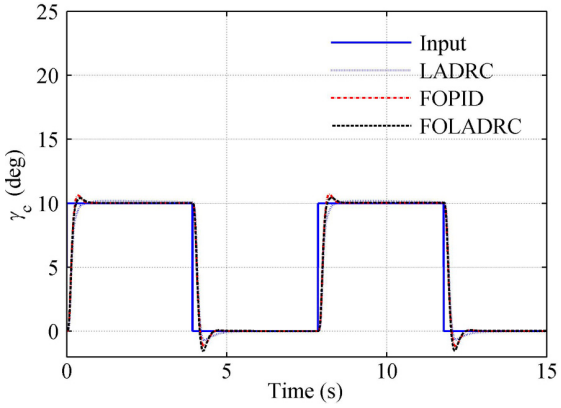

Fig. 18 Output responses of tracking the desired bank angle.

controllers exhibit a better performance in dealing with system coupling than the FOPID controller. The sliding angle tracking errors of the LADRC and FOLADRC

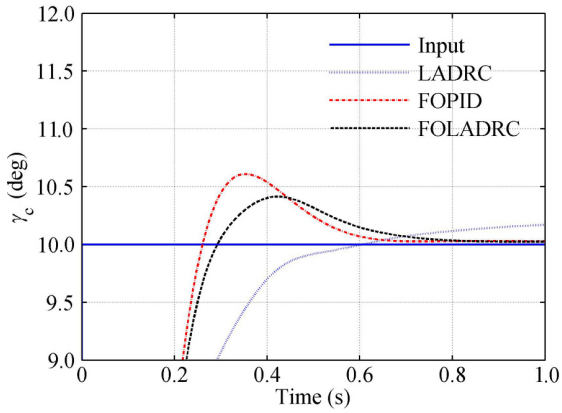

Fig. 19 Output responses of tracking the desired bank angle (partial enlargement).

methods are within 0.1°. Figures 18 and 19 show that the FOLADRC controller has the smallest settling time among the three controllers. From Table 2, we can conclude that the FOLADRC controller achieves the best control performance under the normal operating condition.

4.2 Simulation of the FOLADRC under the actuator fault condition

To test the performance of the FOLADRC for hypersonic vehicles with actuator faults, we set the failure indicator and bias fault for the actuators as an example. The desired attack and bank angles of the control system are still continuous square wave signals with amplitudes of 1° and 10°, respectively. The desired sideslip angle is still zero. The failure indicator for the actuators is assumed as $E_i = \begin{cases} 0, & t \leqslant 2\,\mathrm{s} \\ 0.2, & t > 2\,\mathrm{s} \end{cases}$, and the actuator bias fault is assumed as $\bar{\delta}_i = \begin{cases} 0, & t \leqslant 9\,\mathrm{s} \\ 2 + 0.5\sin(2t), & t > 9\,\mathrm{s} \end{cases}$. The simulation results of the FOLADRC for hypersonic vehicles with actuator faults are shown in Figs. 20–22. The performance parameters (for the second step input signal) of the FOLADRC under the normal operating condition and actuator fault condition are shown in Table 3.

Figures 20–22 show that the FOLADRC method for hypersonic vehicles with actuator faults can still achieve excellent static and dynamic performances. All of the

Table 2 Performance parameters of different controllers.

Method	Settling time of α (5% error band) (s)	Overshoot of α (%)	Maximum of $\lvert\beta\rvert$ (°)	Settling time of γ_c (5% error band) (s)	Overshoot of γ_c (%)
LADRC	0.49	19.7	0.08	0.37	2.0
FOPID	1.05	30.6	0.18	0.41	6.1
FOLADRC	0.38	19.6	0.08	0.25	4.2

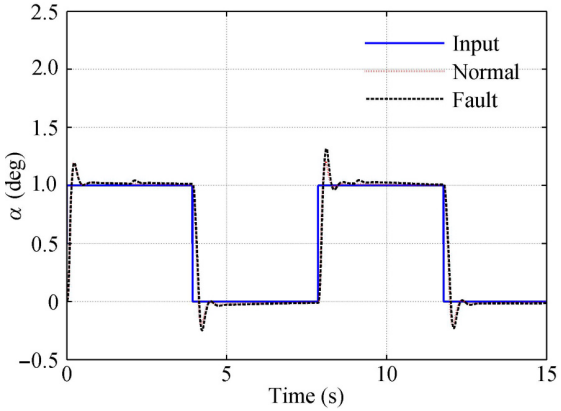

Fig. 20 Attack angle responses of hypersonic vehicles with actuator faults.

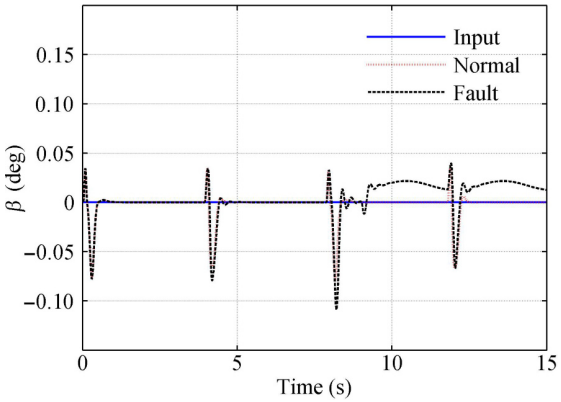

Fig. 21 Sliding angle responses of hypersonic vehicles with actuator faults.

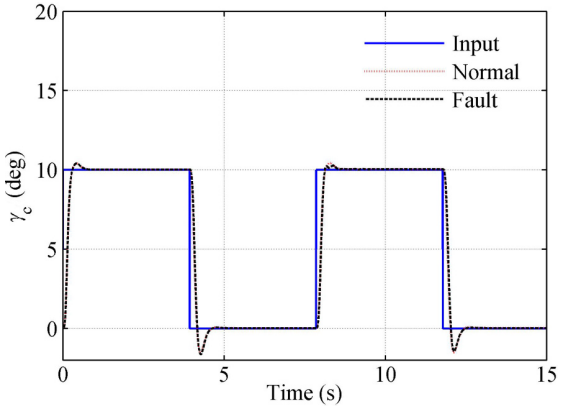

Fig. 22 Bank angle responses of hypersonic vehicles with actuator faults.

state variables can rapidly approach their own stable values. The tracking curves are fine, and the sliding angle responses are small. From Table 3, we can observe that the attitude responses of the FOLADRC under the normal operating condition and actuator fault condition are close. The angle errors between angle responses under the normal operating condition and actuator fault condition of the LADRC, FOPID, and FOLADRC methods for hypersonic vehicles are shown in Figs. 23 – 25. Table 4 shows the average angle errors between the normal operating condition and actuator fault condition.

In Figs. 23 – 25, we can observe that the FOLADRC method can suppress the actuator bias fault and failure indicator for actuators in the hypersonic vehicle model more effectively than the LADRC and FOPID methods. Table 4 shows that the average angle errors of FOLADRC are the smallest, indicating that the FOLADRC method has the highest robustness against actuator faults.

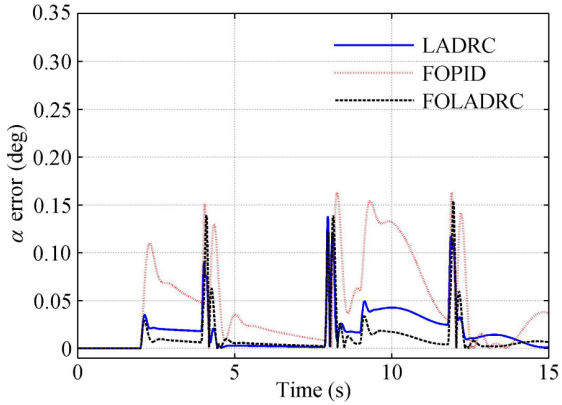

Fig. 23 Attack angle errors of hypersonic vehicles with actuator faults.

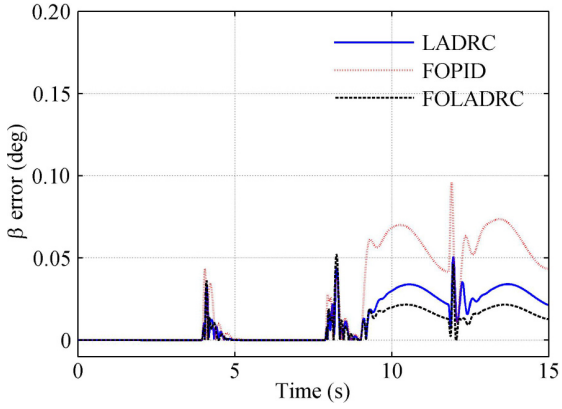

Fig. 24 Sliding angle errors of hypersonic vehicles with actuator faults.

Table 3 Performance parameters under different conditions.

Condition	Settling time of α (5% error band) (s)	Overshoot of α (%)	Maximum of $\lvert\beta\rvert$ (°)	Settling time of γ_c (5% error band) (s)	Overshoot of γ_c (%)
Normal condition	0.370	20.7	0.08	0.244	4.4
Actuator fault	0.393	31.9	0.11	0.249	2.4

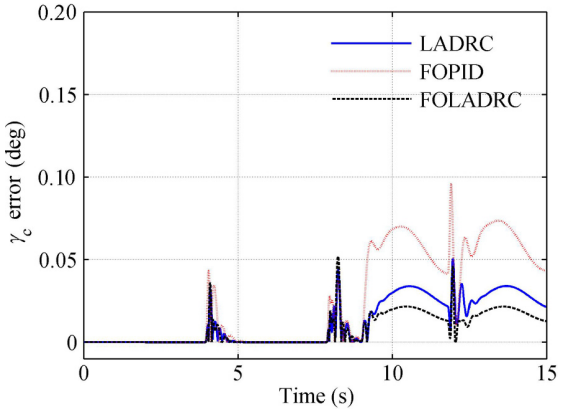

Fig. 25 Bank angle errors of hypersonic vehicles with actuator faults.

Table 4 Average angle errors between the normal operating condition and actuator fault condition.

Method	α (deg)	β (deg)	γ_c (deg)
LADRC	0.019	0.012	0.088
FOPID	0.046	0.025	0.084
FOLADRC	0.012	0.008	0.037

5 Conclusion

In this study, the FOLADRC method, which is the combination of the FOPID method and conventional LADRC method, has been proposed for hypersonic vehicles with actuator faults. The proposed FOLADRC controller combines the advantages of both FOPID and LADRC. Then, the influences of the actuator model on the anti-disturbance capability and parameter tuning of the FOLADRC-based closed-loop control system are analyzed. The frequency-domain analysis method is used to optimize the control parameters of the FOLADRC controller. Finally, the FOLADRC method is applied to the hypersonic vehicle 6-DOF nonlinear model to verify the control effects. The results of the numerical experiments indicated that the FOLADRC method outperforms the FOPID and LADRC methods under both the normal operating condition and actuator fault condition.

Acknowledgment

This work was supported by the National High-Tech Research and Development Program of China (Nos. 11100002017115004 and 111GFTQ2018115005), the National Natural Science Foundation of China (Nos. 61473015 and 91646108), and the Space Science and Technology Foundation of China (No. 105HTKG2019115002). The authors thank the colleagues for their constructive suggestions and research assistance throughout this study.

References

[1] G. Gao and J. Z. Wang, Observer-based fault-tolerant control for an air-breathing hypersonic vehicle model, *Nonlinear Dynamics*, vol. 76, no. 1, pp. 409–430, 2014.

[2] B. Jiang, Y. F. Xu, P. Shi, and Z. Gao, Robust fault-tolerant tracking control for a near-space vehicle using a sliding mode approach, *System and Control Engineering*, vol. 225, no. 8, pp. 1–12, 2011.

[3] Z. Liu, X. Tan, R. Yuan, G. Fan, and J. Yi, Immersion and invariance-based output feedback control of air-breathing hypersonic vehicles, *IEEE Transactions on Automation Science & Engineering,* vol. 13, no. 1, pp. 394–402, 2016.

[4] H. Duan and P. Li, Progress in control approaches for hypersonic vehicle, *Sci. China Technol. Sci.*, vol. 55, no. 10, pp. 2965–2970, 2012.

[5] Y. L. Tian and X. Y. Liu, A deep adaptive learning method for rolling bearing fault diagnosis using immunity, *Tsinghua Science and Technology*, vol. 24, no. 6, pp. 750–762, 2019.

[6] Q. L. Hu, Y. M. Zhang, X. Huo, and B. Xiao, Adaptive integral-type sliding mode control for spacecraft attitude maneuvering under actuator stuck failures, *Chinese Journal of Aeronautics*, vol. 24, no. 1, pp. 32–45, 2011.

[7] G. Y. Lai, C. Y. Wen, Z. Liu, Y. Zhang, C. L. Chen, and S. L. Xie, Adaptive compensation for infinite number of actuator failures/faults using output feedback control, *Information Sciences*, vol. 399, pp. 1–12, 2017.

[8] M. Z. Gao and G. P. Cai, Finite-time H_∞ fault-tolerant control for wing flutter of reentry vehicle subject to input saturation, *International Journal of Control, Automation and Systems*, vol. 15, no. 1, pp. 362–374, 2017.

[9] X. Yu, P. Li, and Y. Zhang, The design of fixed-time observer and finite-time fault-tolerant control for hypersonic gliding vehicles, *IEEE Transactions on Industrial Electronics*, vol. 65, no. 5, pp. 4135–4144, 2018.

[10] Y. Jiang, Q. L. Hu, and G. F. Ma, Adaptive backstepping fault-tolerant control for flexible spacecraft with unknown bounded disturbances and actuator failures, *ISA Transactions*, vol. 49, no. 1, pp. 57–69, 2010.

[11] J. W. Tao, T. Zhang, and Y. F. Nie, Adaptive prescribed performance control for flexible spacecraft with input saturation and actuator misalignment, *Tsinghua Science and Technology*, vol. 24, no. 6, pp. 694–705, 2019.

[12] Y. J. Zhong, Active fault-tolerant tracking control of a quadrotor with model uncertainties and actuator faults, *Frontiers of Information Technology and Electronic Engineering*, vol. 20, no. 1, pp. 95–106, 2019.

[13] J. Q. Han, From PID to active disturbance rejection control, *IEEE Transactions on Industrial Electronics*, vol. 56, no. 3, pp. 900–906, 2009.

[14] Z. Q. Gao, Scaling and bandwidth-parameterization-based controller tuning, in *Proc. of the 2003 American Control Conference*, Denver, CO, USA, 2003, pp. 4989–4996.

[15] I. Podlubny, I. Petráš, B. M. Vinagre, P. O'Leary, and L'. Dorčák, Analogue realizations of fractional order controllers, *Nonlinear Dynamics*, vol. 29, no. 1, pp. 281–296, 2002.

[16] J. Q. Han, From the PID technology to auto-disturbance rejection control technology, (in Chinese), *Control Engineering of China*, vol. 9, no. 3, pp. 13–18, 2002.

[17] C. M. Qin, N. M. Qi, R. Lu, and K. Zhu, ADRC fractional order PID controller design of hypersonic flight vehicle, *Transactions of Nanjing University of Aeronautics & Astronautics*, vol. 3, no. 5, pp. 466–469, 2011.

[18] J. Song, L. Wang, G. B. Cai, and X. Q. Qi, Nonlinear fractional order proportion-integral-derivative active disturbance rejection control method design for hypersonic vehicle attitude control, *Acta Astronautica*, vol. 111, pp. 160–169, 2015.

[19] J. Song, J. M. Lin, L. Wang, X. Wang, and X. H. Guo, Nonlinear FOPID and active disturbance rejection hypersonic vehicle control based on DEM biogeograph, *Journal of Aerospace Engineering*, vol. 30, no. 6, pp. 1–10, 2017.

[20] Q. X. Wu, M. W. Sun, Z. H. Wang, and Z. Q. Chen, Practical solution to efficient flight path control for hypersonic vehicles, *Transactions of the Japan Society for Aeronautical and Space Sciences*, vol. 59, no. 4, pp. 195–204, 2016.

[21] J. Y. Tian, S. F. Zhang, Y. H. Zhang, and T. Li, Active disturbance rejection control based robust output feedback autopilot design for airbreathing hypersonic vehicles, *ISA Transactions*, vol. 74, no. 2018, pp. 45–59, 2018.

[22] J. D. Shaughnessy, S. Z. Pinckney, J. D. McMinn, and C. I. Cruz, Hypersonic vehicle simulation model: Winged-cone configuration, Report, NASA Langley Research Center, Hampton, VA, USA, 1990.

[23] S. Keshmiri, R. Colgren, and M. Mirmirani, Development of an aerodynamic database for a generic hypersonic air vehicle, In *Proc. of the AIAA Guidance, Navigation, and Control Conference and Exhibit*, San Francisco, CA, USA, 2005, pp. 1–21.

Ke Gao received the BS degree from Beihang University, Beijing, China, in 2010. He is currently pursuing the PhD degree in Beihang University, Beijing, China. His research interest includes active disturbance rejection control technology, fractional-order PID control, fault diagnosis and fault tolerant control, and aircraft control system.

Jia Song received the BS, MS, and PhD degrees from Harbin Engineering University, Harbin, China, in 2005, 2008, and 2009, respectively. She is currently an associate professor with the School of Astronautics, Beihang University, Beijing, China. Her research interests include fault diagnosis and fault tolerant control, data driven control, active disturbance rejection control technology, and the theory of intelligent control and application.

Xu Wang received the PhD degree from Department of Jet Propulsion, Beihang University, Beijing, China, in 1990. He is currently an associate professor in the School of Aerospace, Mechanical and Manufacturing Engineering, RMIT University. His research interests include vibro-acoustic study using deterministic and statistical methods, vehicle noise and vibration mitigation and refinement, and vibration energy harvesting using piezoelectric materials and electromagnetic devices.

Huifeng Li received the BS and PhD degrees from Xi'an Jiaotong University, Xi'an, China, in 1991 and 1998, respectively. She is currently a professor with the School of Astronautics, Beihang University, Beijing, China. Her research interests include aircraft guidance and control technology.